SEMARAK ILMU PUBLISHING

Journal of Advanced Research in Fluid Mechanics and Thermal Sciences

Journal homepage:
https://semarakilmu.com.my/journals/index.php/fluid_mechanics_thermal_sciences/index
ISSN: 2289-7879

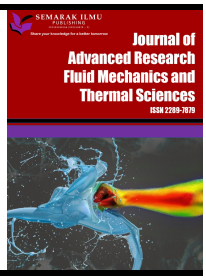

Numerical investigation of heat transfer enhancement and flow characteristics of nanofluid around two tandem cylinders

Ridha Mebrouk[1,*], Issam Rezaiguia[1], Mahfoud Kadja[2], Aissa Abidi Saad[1]

[1] Department of Drilling and Oil Mechanics Building, University of kasdi Maerbah Ouargla, 30000 Ouargla, Algeria
[2] Laboratory of Renewable Energies and Sustainable Development, Department of Mechanical Engineering, University of Frères Mentouri,25000 Constantine, Algeria

ARTICLE INFO

Article history:
Received 2 December 2025
Received in revised form 12 January 2026
Accepted 16 January 2026
Available online 20 January 2026

Keywords:
Computational Fluid Dynamics (CFD) ; Nanofluid; Vortex shedding; Heat transfer; Nusselt number; Drag coefficient; Lift coefficient

ABSTRACT

This study presents a numerical investigation of unsteady laminar flow and convective heat transfer of a Cu–water nanofluid, modeled using a single-phase homogeneous approach, around two tandem circular cylinders placed in a semi-confined channel. The unsteady laminar flow is simulated using the finite volume method implemented in ANSYS Fluent. The working fluid is a Cu–water nanofluid with a Prandtl number of 7, and nanoparticle volume fractions ranging from 0% to 6%, while the Reynolds number is fixed at 100. The study examines various center-to-center spacing ratios between 2 and 5, keeping the blockage ratio constant at 0.25. Detailed analyses of the flow and thermal fields are performed using streamlines, vorticity contours, and temperature distributions. The results indicate that both the spacing ratio and nanoparticle concentration strongly influence the hydrodynamic forces and heat transfer characteristics. At a nanoparticle volume fraction of 6%, the average Nusselt number is enhanced by approximately 8% for the upstream cylinder and 28% for the downstream cylinder compared to pure water. The enhancement becomes more significant at larger cylinder separations, whereas the critical spacing ratio, around 3.9D, remains essentially unchanged when the base fluid is replaced with the nanofluid. These findings offer valuable insight into how nanoparticle loading and cylinder spacing can be optimized to improve convective heat transfer in compact heat exchanger applications. It should be noted that the nanofluid is treated as a homogeneous fluid with constant thermophysical properties, which neglects possible particle slip, agglomeration, and non-uniform distribution effects.

1. Introduction

The investigation of fluid flow and heat transfer around bluff bodies has remained a topic of considerable research interest owing to its significance in various engineering applications, including gas turbine cooling, polymer extrusion, and heat exchanger optimization. Among the different bluff body geometries—such as circular, square, and trapezoidal—tandem cylinder configurations are particularly complex due to their intricate vortex dynamics and flow interactions. The pioneering studies of Igarashi [1–2] and Zdravkovich [3] provided the foundation for understanding vortex

* *Corresponding author.*
E-mail address: ridhamebrouk@gmail.com

https://doi.org/10.37934/arfmts.137.1.117

shedding mechanisms and wake interactions between cylinders. Subsequent works extended this understanding by addressing parameters such as vortex formation, fluid-induced vibrations, drag and lift behavior, and associated heat transfer processes. Comprehensive reviews and datasets summarizing these findings for various cross-sectional shapes—including circular, triangular, and square bodies—have been compiled in the literature (Chung et al., [4] ; Rosales et al., [5]; Ding et al., [6]; Mahir et al., [7]; Sohankar et al.,[8]; Sumner, [9]; Jiang et al., [10]; Harichandan et al., [11]; Dhiman et al., [12]). Nevertheless, the majority of these contributions have focused primarily on conventional fluids, such as air and water.

More recent investigations have expanded the research scope by incorporating non-traditional geometries and boundary conditions. Rajpoot et al., [13] numerically examined the effects of cylinder orientation on forced convection around a semi-circular cylinder near a stationary wall under shear flow, showing a strong correlation between angular position and heat transfer enhancement. Similarly, Gupta et al., [14] analyzed mixed convection flow past tandem semi-circular cylinders within a vertical channel and emphasized the role of dimensionless parameters—including Reynolds, Prandtl, and Richardson numbers, along with the spacing ratio—in dictating drag and heat transfer characteristics. Moreover, Talaat Abdelhamid et al., [15] reported that curved corners on an isothermal cylinder subjected to varying attack angles could enhance thermal performance by up to 12.9%. Collectively, these results confirm that geometrical alterations and cylinder interactions substantially influence flow patterns, the Strouhal number, and overall heat transfer efficiency.

Parallel to these geometric studies, nanofluids have emerged as advanced working fluids owing to their superior thermal conductivity compared with conventional media such as oil, water, and ethylene glycol. A considerable number of publications (Mahmoodi et al., [16]; Soltanipour et al., [17]; Fallah et al., [18] ; Arumuga et al., [19]) have demonstrated the potential of nanofluids in enhancing convective heat transfer. Mahfouz and Badr., [20] investigated oscillating cylinders at Reynolds numbers between 40 and 200 and observed significant increases in Nusselt number and vorticity when nanofluids were used. Additional studies on flow over square cylinders using Al_2O_3–water nanofluids revealed that even low nanoparticle concentrations improve heat transfer efficiency by reducing the thermal boundary layer thickness. Similar observations were reported by Farooji et al., [21], who numerically confirmed enhanced convective performance in nanofluid flows past isolated square cylinders. Altogether, these findings demonstrate the beneficial influence of nanoparticle dispersion in improving the convective and thermal behavior of bluff-body systems.

Despite this progress, limited attention has been devoted to the combined effect of nanofluids and tandem cylinder configurations, particularly in confined or semi-confined domains. This gap is noteworthy, as the hydrodynamic interaction between successive cylinders strongly modifies wake topology, force coefficients, and temperature distribution. A recent study by Ali Azad et al., [22] applied the Smoothed Particle Hydrodynamics (SPH) method to evaluate nanofluid flow in differently shaped channels and achieved up to 48.8% improvement in local heat transfer by optimizing obstacle placement. Nonetheless, the simultaneous influence of nanoparticle concentration and cylinder spacing in tandem arrangements remains insufficiently characterized.

Unlike previous studies that primarily focus on either tandem cylinder flow using conventional fluids or nanofluid heat transfer around isolated bluff bodies, the present work explicitly investigates the coupled effects of nanoparticle loading and inter-cylinder spacing in a semi-confined tandem cylinder configuration. The novelty of this study lies in clarifying how nanofluid-induced modifications of momentum and thermal diffusion interact with wake interference mechanisms, particularly in the downstream cylinder. Furthermore, the study demonstrates that nanoparticle addition enhances heat transfer without altering the critical spacing ratio governing flow regime transition, which has

not been clearly reported in earlier investigations. These findings contribute to a deeper physical understanding of nanofluid-assisted heat transfer in interacting bluff-body systems.

2. Governing Equations

The configuration and coordinate system of the flow are illustrated in Figure 1. In order to describe the flow, the time-dependent, two-dimensional Navier-Stokes and energy equations of an incompressible nanofluid are utilized. It is assumed that the base fluid (water) and the nanoparticles (Cu) are in thermal equilibrium. Furthermore, it is assumed that all of the physical properties of the nanofluid (as detailed in Table 1) remain constant. In the context of laminar flow, the dimensions of the continuity, momentum, and thermal energy equations can be expressed as follows (Sarkar et al., [23]):

- The continuity equation

$$\frac{\partial u}{\partial x}+\frac{\partial v}{\partial y}=0 \tag{1}$$

- The momentum equation in the x direction

$$\frac{\partial u}{\partial t}+u\frac{\partial u}{\partial x}+v\frac{\partial u}{\partial y}=-\frac{\rho_{f,ref}}{\rho_{nf,ref}}\frac{\partial p}{\partial x}+\frac{\mu_{eff}}{\nu_f\rho_{nf,ref}}\frac{1}{Re}\left(\frac{\partial^2 u}{\partial x^2}+\frac{\partial^2 u}{\partial y^2}\right) \tag{2}$$

- The momentum equation in the y direction

$$\frac{\partial v}{\partial t}+u\frac{\partial v}{\partial x}+v\frac{\partial v}{\partial y}=-\frac{\rho_{f,ref}}{\rho_{nf,ref}}\frac{\partial p}{\partial y}+\frac{\mu_{eff}}{\nu_f\rho_{nf,ref}}\frac{1}{Re}\left(\frac{\partial^2 v}{\partial x^2}+\frac{\partial^2 v}{\partial y^2}\right) \tag{3}$$

- The energy equation

$$\frac{\partial \theta}{\partial t}+u\frac{\partial \theta}{\partial x}+v\frac{\partial \theta}{\partial y}=\frac{\alpha_{nf}}{\alpha_f}\frac{1}{RePr}\left(\frac{\partial^2 \theta}{\partial x^2}+\frac{\partial^2 \theta}{\partial y^2}\right) \tag{4}$$

The dimensionless velocity components along the xxx and yyy directions are denoted by u and v, respectively, while θ represents the dimensionless fluid temperature.

The Reynolds number is defined as $R_e=\frac{\rho_f u_{avg} D}{\mu_f}$, where ρ_f is the base fluid density, u_{avg} is the average inlet velocity, D is the cylinder diameter, and μ_f is the dynamic viscosity of the based fluid . The Prandtl number is given by $Pr=\mu_f c_{pf}/k_f$, where c_{pf} and k_f are the specific heat capacity and thermal conductivity of the base fluid, respectively denotes the thermal diffusivity of the fluid. Subscripts f, nf, ref refer to the base fluid, nanofluid, and α properties evaluated at the reference temperature, respectively.

The gap ratio (denoted as GR) is defined as the ratio of the spacing between the centerlines of the cylinders to their diameter, expressed as GR=S/D, where S represents the aforementioned spacing between the centerlines of the cylinders. The value was selected from the interval 2 to 5. The upstream and downstream distances of the computational domain, respectively denoted as Xu and XD, are given by values of 10D and 25D. The blockage ratio of the computational domain is defined as follows: β is equal to D divided by H, which is equal to 0.25.

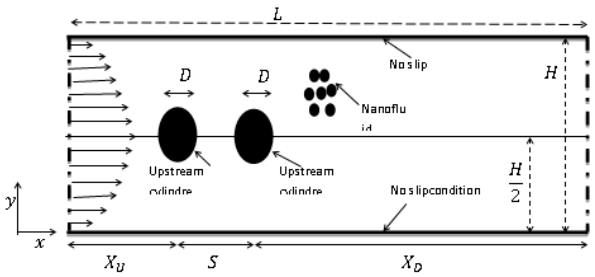

Fig. 1. Computational domain of the two cylinders configuration

The boundary conditions for the inlet, outlet, walls, and surface of the cylinders can be expressed as follows:

For the inlet: A fully developed $2-\mathrm{D}$ parabolic velocity profile:

$$\mathrm{u}=1.5\mathrm{u}_{\mathrm{avg}}\left(1-\left(1-\frac{2\mathrm{Dy}}{\mathrm{H}}\right)^{2}\right) \tag{5}$$

Where $0\leq \mathrm{y}\leq \mathrm{H}/\mathrm{D}$, $\mathrm{v}=0$, $\mathrm{T}=\mathrm{T}_{\infty}$ (6)

For the outlet:

$$\frac{\partial \mathrm{u}}{\partial \mathrm{x}}=\frac{\partial \mathrm{v}}{\partial \mathrm{y}}=\frac{\partial \mathrm{T}}{\partial \mathrm{x}}=0 \tag{7}$$

For the bottom and top walls:

$$\frac{\partial \mathrm{T}}{\partial \mathrm{x}}=0,\ \mathrm{u}_{\mathrm{x}}=\mathrm{u}_{\mathrm{v}}=0 \tag{8}$$

For the cylinders walls;

$$\mathrm{u}_{\mathrm{x}}=\mathrm{u}_{\mathrm{v}}=0,\mathrm{T}=\mathrm{T}_{\mathrm{w}} \tag{9}$$

Where $\mathrm{u}_{\mathrm{avg}}$, T_{∞} are the average velocity and stream temperature respectively and T_{w} is the cylinder wall temperature.

One of the key parameters in the present study is the Reynolds number, Eq. 10

$$\mathrm{R}_{\mathrm{e}}=\frac{\rho_{\mathrm{f}}\mathrm{u}_{\mathrm{avg}}\mathrm{D}}{\mu_{\mathrm{f}}} \tag{10}$$

This study focuses on the impact of spatial parameters, specifically the distance between cylinders and the volume fraction of nanoparticles, on the dynamic characteristics of flow phenomena. These include the drag and lift coefficients (equations 11 and 12) and the transfer of heat from cylinders to nanofluids.

The present investigation is intentionally restricted to a laminar flow regime at Re = 100 and Pr = 7 in order to isolate the fundamental interactions between wake dynamics and nanofluid thermal transport mechanisms. While this limitation reduces direct applicability to turbulent industrial flows, it allows a clear interpretation of the physical processes governing heat transfer enhancement in tandem cylinder configurations. The results therefore serve as a baseline for future extensions to higher Reynolds numbers and different Prandtl numbers relevant to practical engineering systems

The overall mean drag and mean lift coefficient are mathematically defined as:

$$\mathrm{C}_{\mathrm{D}}=\frac{\mathrm{F}_{\mathrm{D}}}{\frac{1}{2}\rho \mathrm{u}_{\mathrm{avg}}^{2}\mathrm{D}} \tag{11}$$

$$\mathrm{C}_{\mathrm{L}}=\frac{\mathrm{F}_{\mathrm{L}}}{\frac{1}{2}\rho \mathrm{u}_{\mathrm{avg}}^{2}\mathrm{D}} \tag{12}$$

Where, F_{D} and F_{L} are the lift and drag force components in the longitudinal and transverse directions respectively.

The local Nusselt number is defined based on the cylinder diameter D as the length scale:

$$-\frac{k_{eff}}{k_f}\frac{\partial T}{\partial n}\Big|_w = h_\theta(T_w - T_\infty)\ ,\ Nu_\theta = \frac{h_\theta D}{k_f} \tag{13}$$

Where, h_θ is the local surface heat transfer coefficient, and n is the direction perpendicular to the cylinder wall. The average Nusselt number at the cylinder wall is calculated by integration of the local Nusselt number over the cylinder surface.

$$\overline{N_u} = \frac{1}{2\pi}\int_{\theta=0}^{\theta=2\pi} Nu_\theta d\theta \tag{14}$$

3. Thermophysical Properties of Nanofluids

The thermophysical properties, obtained from [23] for pure water and copper at room temperature are tabulated in Table 1. We used the Brinkman model to determine the effective viscosity of the nanofluid. The expression used is given by (Xuan et al., [24]):

$$\mu_{eff} = \frac{\mu_f}{(1-\varphi)^{2.5}} \tag{15}$$

Where φ is the nanoparticle volume fractions and is given as:

$$\varphi = \frac{\text{volume of nanoparticles}}{\text{total volume of solution}}$$

This correlation was experimentally validated by (Xuan et al., [24]) for both oil–water and water–copper nanofluids in the range of temperatures 20–50 ^{0}C. Their experimental results were found to be in good match with Brickman's theory.

The effective density of the nanofluid at the reference temperature is given by [24]:

$$\rho_{nf,ref} = \varphi\rho_{nf,ref} + (1-\varphi)\rho_{f,ref} \tag{16}$$

The effective heat capacitance of the nanofluid at the reference temperature was calculated by the equation given by (Xuan et al., [24]) as:

$$(\rho C_p)_{nf,ref} = \varphi(\rho C_p)_s + (1-\varphi)(\rho C_p)_f \tag{17}$$

The Maxwell–Garnett's (MG) model Brinkman was used for determining the effective thermal conductivity of the nanofluids. In the case of nanoparticles with aspherical shape, it is given by the formula [29]:

$$k_{eff} = k_f\left[\frac{(k_s+2k_f)-2\varphi(k_f-k_s)}{(k_s+2k_f)+\varphi(k_f-k_s)}\right] \tag{18}$$

The thermal diffusivity of the nanofluid is given by:

$$\alpha_{nf} = \frac{k_{eff}}{(\rho C_p)_{nf,ref}} \tag{19}$$

Table 1
Thermophysical properties of pure water and copper at room temperature[25].

Material	ρ	μ	k	C_p
Water	997.1	0.001	0.6	4179
Copper	8954	-	400	383

The present study assumes constant thermophysical properties for the nanofluid, thermal equilibrium between the base fluid and nanoparticles, and neglects particle agglomeration, Brownian motion, and slip velocity effects. These assumptions are commonly adopted in single-phase nanofluid modeling at low particle concentrations; however, they may lead to deviations when higher concentrations or turbulent regimes are considered.

4. Numerical Methods and Simulation Conditions

In this study, the governing flow and energy equations with their boundary conditions have been solved numerically by the finite volume method using the ANSYS Fluent CFD code. The ANSYS work-bench was used to generate structured quadrilateral cells of uniform and non uniform grid spacing as shown in Figure 2.

Fig. 2. Magnified view of a grid structure around the two tandem cylinders ($\mathrm{GR} = 4$)

The governing equations for incompressible flow were solved using a two-dimensional, unsteady, laminar, segregated solver on a collocated grid arrangement. The velocity-pressure coupling was achieved through the Semi-Implicit Method for Pressure-Linked Equations (SIMPLE) algorithm. Convective terms in the momentum and energy equations were discretized using the QUICK (Quadratic Upstream Interpolation for Convective Kinematics) scheme, while a second-order implicit time integration was applied to the temporal terms. A dimensionless time step of $\Delta t = 0.01$ was adopted, based on a time-step sensitivity study, which confirmed that smaller values have negligible impact on the global flow and heat transfer results.

The resulting system of algebraic equations was solved in ANSYS Fluent using the Gauss-Seidel point-by-point iterative method in combination with an algebraic multigrid technique. The inlet velocity was defined via a user-defined function (UDF) within Fluent.

For all simulations, the computational domain was discretized using a structured mesh, with finer clustering near the cylinder surfaces and along the top and bottom walls to accurately resolve steep gradients in velocity, temperature, and pressure. The clustering density was carefully chosen to balance accuracy with computational cost. A grid independence study, conducted at GR = 4, Re = 100, and $\phi = 4\%$, compared two quadrilateral grids with different numbers of points along the cylinder surfaces (Ni) and different near-wall spacing ratios (δ/D). The results, summarized in Table 2, indicate that Grid 2 (Ni = 200, $\delta/D = 0.005$) provides sufficient resolution for the present numerical simulations.

Table 2
Mesh independence study at Re=100 and GR=4 for $\varphi = 4\%$ and Pr=7.

Mesh Title	Number of mesh elements	C_{D1}	C_{D2}	Nu_1	Nu_2
Mesh 1	22600	2.797	1.214	16.455	15.035
Mesh 2	31400	2.8030	1.235	16.476	15.006
Mesh 3	43600	2.8031	1.236	16.477	15.005

A systematic grid independence study and time-step sensitivity analysis were conducted to ensure numerical accuracy. Three progressively refined structured meshes were tested, and the results demonstrated negligible variations in drag, lift, and average Nusselt numbers beyond the selected grid. The adopted time step (Δt = 0.01) was verified to provide time-accurate solutions without affecting the global flow and heat transfer characteristics. Additionally, the numerical methodology was validated against benchmark numerical data for both single and tandem cylinder configurations, showing excellent agreement with published results.

5. Results and Discussion

This section commences with an account of the validation study, which is then followed by a discussion of the results obtained through numerical simulation. These are displayed in the form of streamline, vorticity, and isotherm contours, accompanied by the drag coefficient, the lift coefficient, the local Nusselt number, and the surface average Nusselt number.

5.1 Validation study

Before addressing the main computational analysis, a comprehensive validation process was carried out to ensure the reliability and accuracy of the present numerical results. This validation involved reproducing benchmark cases related to the flow and heat transfer characteristics of single and tandem heated circular cylinders in both confined and unconfined channels. The corresponding comparisons of flow and thermal parameters with previously published data are summarized in Tables 3 and 4 and illustrated in Figure 3.

In the first validation case, an unconfined domain containing a single heated circular cylinder was examined. The mean drag coefficient, lift coefficient, and average Nusselt number obtained in the present simulation were compared with the reference results reported by Mahir et al. [7] and Harimi et al. [26], as listed in Table 3 for Re = 100 and Pr = 0.7.

The second validation case considered a confined configuration with two identical circular cylinders arranged in tandem, exposed to both uniform and parabolic inlet velocity profiles at a gap ratio of GR = 4. For Re = 100 and Pr = 0.7, the comparison between the computed mean drag and lift coefficients and the average Nusselt numbers for the upstream and downstream cylinders is presented in Table 4 and Figure 3.

Overall, the obtained results exhibit a strong correlation with previously published numerical data, particularly those reported by Dwivedi et al. [27], confirming the robustness and precision of the present computational approach.

Table 3
Comparison between the present and literature values of the mean drag, lift coefficients and average Nusselt number for a single unconfined cylinder at $\mathrm{Re} = 100$ and $\mathrm{P} = 0.7$.

References	$\mathbf{C_D}$	$\mathbf{C_L}$	$\overline{\mathbf{Nu}}$
Present study	1.357	0.349	5.168
Mahir& Alta, [7]	1.368±0.029	±0.343	5.179±0.003
Harimi and al, [26]	1.344±0.007	±0.306	5.061

Table 4
Comparison between the present and literature values of the mean drag, lift coefficients and average Nusselt number for two tandem confined cylinders at $\mathrm{Re} = 100$ and $\mathrm{Pr} = 0.7$.

References	$\mathrm{C_{D1}}$	$\mathrm{C_{D2}}$	$\mathrm{C_{L1}}$	$\mathrm{C_{L2}}$	$\mathrm{Nu_1}$	$\mathrm{Nu_2}$
Present study	2.968	2.483	1.246	3.044	6.368	5.260
Dwivedi and al, [27]	2.97	2.49	1.242	3.047	6.385	5.300

(a) Dwivedi and al., [27] (b) Present study

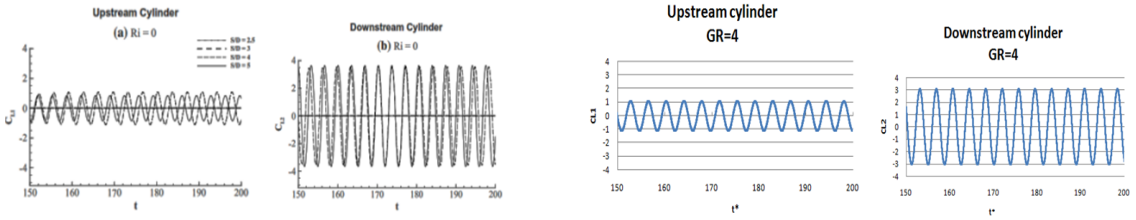

Fig. 3. Comparison between the present and literature values of the time histories of lift coefficients and for a two tandem confined cylinders at $\mathrm{Re} = 100$, GR=4 and $\mathrm{Pr} = 0.7$.

5.2 Streamlines, vorticity and isotherms contours

Figure 4 illustrates the instantaneous streamlines around the two tandem circular cylinders for different gap ratios (GR = 2–5) and nanoparticle volume fractions ranging from ϕ = 0% to 6% at Re = 100. The flow structure is strongly influenced by the gap ratio, while the presence of nanoparticles mainly affects the wake intensity and stability rather than altering the overall flow topology.

At the smallest spacing (GR = 2), the flow exhibits a quasi-steady behavior for all nanoparticle concentrations. The shear layers emanating from the upstream cylinder reattach onto the downstream cylinder, forming an extended recirculation region between the cylinders. This strong wake interference suppresses vortex shedding, leading to a relatively stable flow pattern. Increasing the nanoparticle volume fraction slightly thickens the shear layers and weakens the recirculation strength, but no qualitative change in the flow regime is observed.

When the gap ratio is increased to GR = 3, the interaction between the wakes becomes weaker, and small-scale vortical structures begin to appear downstream of the second cylinder. The onset of unsteady behavior is more noticeable for higher nanoparticle concentrations, where the enhanced effective viscosity of the nanofluid tends to dampen vortex intensity while preserving the general wake configuration.

At GR = 4, a clear transition to a fully unsteady flow regime is observed. Periodic vortex shedding develops behind both cylinders, and the wake interaction becomes more complex. The downstream cylinder is strongly influenced by the vortices shed from the upstream one, resulting in an asymmetric

wake structure. The addition of nanoparticles slightly stabilizes the flow by reducing vortex strength and elongating the recirculation zones, although the shedding frequency and overall wake pattern remain similar to those of the base fluid.

For the largest spacing (GR = 5), the two cylinders behave almost independently. Well-defined and alternating vortices are shed from each cylinder, and the wake interaction is significantly reduced. The influence of nanoparticle loading is mainly reflected in smoother streamline patterns and weaker vortical structures, indicating enhanced momentum diffusion. Despite these effects, the critical gap ratio associated with the transition between flow regimes remains essentially unchanged with increasing nanoparticle concentration.

Overall, the results demonstrate that the gap ratio governs the wake interaction mechanism and flow regime transition, whereas the nanoparticle volume fraction primarily modulates the wake strength and stability without significantly affecting the critical spacing between the cylinders.

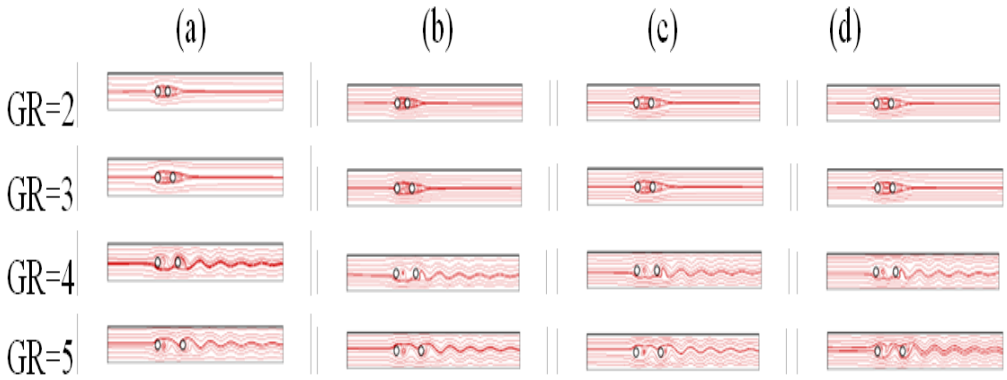

Fig. 4. Streamlines for various gap ratios at (a) $\varphi = 0\%$, (b) $\varphi = 2\%$, (c) $\varphi = 4\%$ and (d) $\varphi = 6\%$.

Figure 5 presents the instantaneous vorticity contours around the tandem circular cylinders for different gap ratios (GR = 2–5) and nanoparticle volume fractions (ϕ = 0–6%) at Re = 100. The vorticity distribution clearly highlights the wake interaction mechanisms and the transition from steady to unsteady flow regimes as the cylinder spacing increases.

For the smallest spacing (GR = 2), strong wake interference is observed, characterized by an elongated recirculation zone between the cylinders and high vorticity layers attached to the downstream cylinder. The shear layers shed from the upstream cylinder impinge directly on the downstream one, suppressing the formation of alternating vortices. Increasing the nanoparticle concentration leads to a noticeable attenuation of vorticity magnitude, which can be attributed to the enhanced effective viscosity and momentum diffusion of the nanofluid, while the overall flow structure remains unchanged.

At GR = 3, the wake interaction weakens and localized vortical structures start to develop downstream of the second cylinder. The vorticity contours reveal the onset of periodic vortex shedding, although the shedding process is still partially constrained by the upstream wake. Higher nanoparticle volume fractions reduce the intensity of the vortices and smooth the vorticity gradients, indicating a stabilizing effect on the flow.

When the gap ratio reaches GR = 4, a fully developed unsteady regime emerges. Distinct and alternating vortices are shed from both cylinders, and the wake interaction becomes highly dynamic. The downstream cylinder experiences strong modulation by the vortices generated upstream, resulting in complex vorticity patterns. The presence of nanoparticles slightly weakens the vorticity cores and elongates the wake structures, but does not alter the shedding mechanism or the transition gap ratio.

For the largest spacing (GR = 5), the two cylinders behave nearly independently, with well-organized vortex streets forming behind each cylinder. The vorticity contours show a reduction in wake interference and a more symmetric shedding pattern. Increasing the nanoparticle concentration further diminishes vorticity intensity and promotes smoother wake structures, reflecting enhanced viscous diffusion. However, the qualitative wake dynamics and shedding frequency remain largely unaffected.

Overall, the vorticity contours confirm that the gap ratio plays a dominant role in governing wake interaction and flow regime transition, whereas the nanoparticle volume fraction mainly influences the strength and coherence of the vortical structures without significantly shifting the critical spacing between the cylinders.

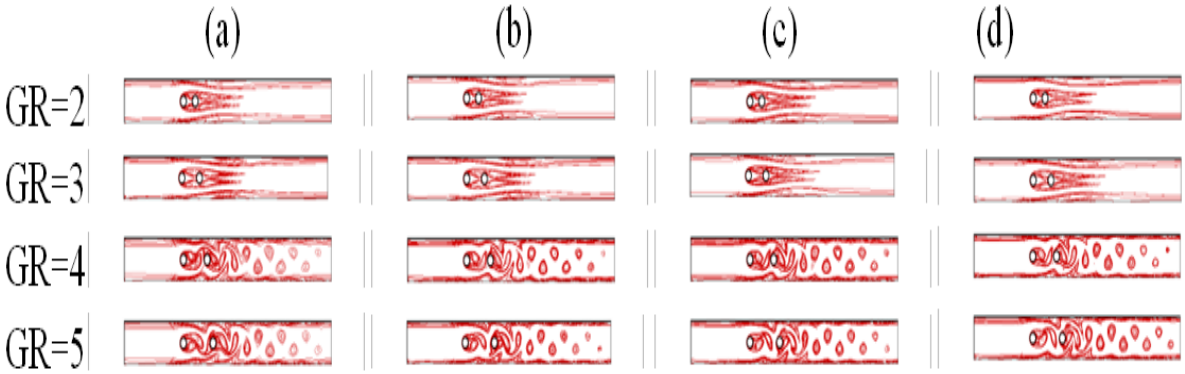

Fig. 5. Vorticity contours for various gap ratios at (a) $\varphi = 0\%$, (b) $\varphi = 2\%$, (c) $\varphi = 4\%$ and (d) $\varphi = 6\%$.

Figure 6 depicts the time-averaged isotherms around the tandem circular cylinders for different gap ratios (GR = 2–5) and nanoparticle volume fractions (ϕ = 0–6%) at Re = 100. The thermal field is strongly coupled with the wake dynamics and flow regime identified in the streamline and vorticity analyses.

At the smallest spacing (GR = 2), the thermal field is dominated by strong wake interference between the two cylinders. The isotherms are densely packed near the upstream cylinder, indicating a relatively thick thermal boundary layer and limited convective transport. The downstream cylinder is immersed in the warm wake of the upstream one, resulting in weaker temperature gradients and reduced heat transfer enhancement. Increasing the nanoparticle concentration slightly intensifies the thermal gradients near the cylinder surfaces due to the higher effective thermal conductivity of the nanofluid, but the overall thermal pattern remains largely unchanged because of the suppressed vortex activity.

For GR = 3, the partial separation of the wakes leads to a moderate distortion of the isotherms downstream of the second cylinder. The onset of unsteady flow promotes enhanced thermal mixing, particularly around the downstream cylinder. Higher nanoparticle volume fractions produce more compact isotherms near the cylinder surfaces, reflecting improved heat diffusion and convection, although the thermal wake interaction is still significant.

At GR = 4, a pronounced change in the thermal field is observed. The fully developed vortex shedding enhances fluid mixing in the wake region, resulting in strongly distorted and periodically stretched isotherms behind both cylinders. The downstream cylinder benefits substantially from the incoming vortices, leading to thinner thermal boundary layers and steeper temperature gradients. The addition of nanoparticles further amplifies this effect, yielding a marked enhancement in convective heat transfer.

For the largest spacing (GR = 5), the cylinders behave almost independently from a thermal perspective. Well-developed thermal wakes form behind each cylinder, and the isotherms exhibit clear periodicity associated with vortex shedding. The influence of nanoparticle loading becomes more pronounced, as the combined effects of increased thermal conductivity and vigorous wake-induced mixing produce thinner thermal boundary layers and more uniform temperature distributions in the wake.

Overall, the time-averaged isotherms confirm that the enhancement of heat transfer is primarily driven by wake-induced mixing at larger gap ratios, while nanoparticle addition acts as a secondary mechanism that intensifies thermal gradients without altering the fundamental thermal interaction regime. This explains the significantly higher Nusselt number observed for the downstream cylinder at larger spacings

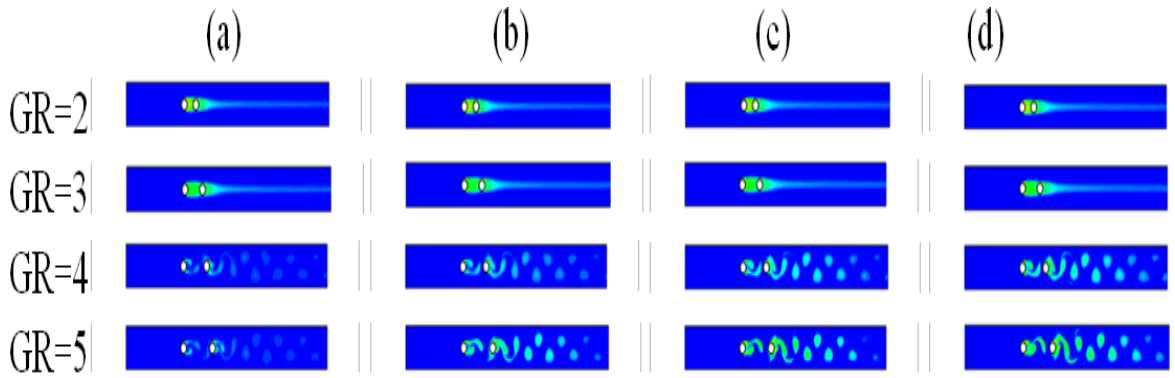

Fig. 6. Time averaged isotherms for various gap ratios at (a) $\varphi = 0\%$, (b) $\varphi = 2\%$, (c) $\varphi = 4\%$ and (d) $\varphi = 6\%$.

5.3 Variation of lift and drag coefficients with volume fractions and gap ratio

Figures 7 and 8 display the time histories of the lift and drag coefficients (CL and CD) for two tandem circular cylinders at Re = 100 and for gap ratios ranging from GR = 2 to 5. At GR = 2, the amplitude variations of CL and CD remain relatively small, which corresponds to the absence of a well-developed vortex street behind the cylinders, as previously shown in Figure 5. The upstream cylinder exhibits smaller oscillations in both lift and drag compared with the downstream one. At this spacing, no distinct vortex shedding occurs from either cylinder; instead, the fluctuations in CL primarily result from the unsteady motion of the shear layers separating from the cylinder surfaces.

For the downstream cylinder, the observed variations in CL are mainly attributed to the periodic reattachment of the upstream cylinder's shear layers combined with the vortices that detach from its own surface. When the gap ratio exceeds GR > 3, the aerodynamic forces acting on the downstream cylinder become significantly stronger than those on the upstream one, as the vortex shedding becomes more organized and energetic. This increase in the intensity of the wake interaction markedly amplifies both drag and lift fluctuations.

A pronounced transition in the flow regime and the associated hydrodynamic forces occurs at approximately GR= 4, which corresponds to the well-known critical spacing ratio where the flow structure changes from steady to unsteady behavior. Additionally, it can be observed that the amplitudes of CL and CD for both cylinders increase progressively with the nanoparticle volume fraction (ϕ). This trend is linked to the thickening of the hydrodynamic boundary layer as ϕ increases, which enhances momentum exchange near the cylinder surfaces and amplifies the overall force oscillations.

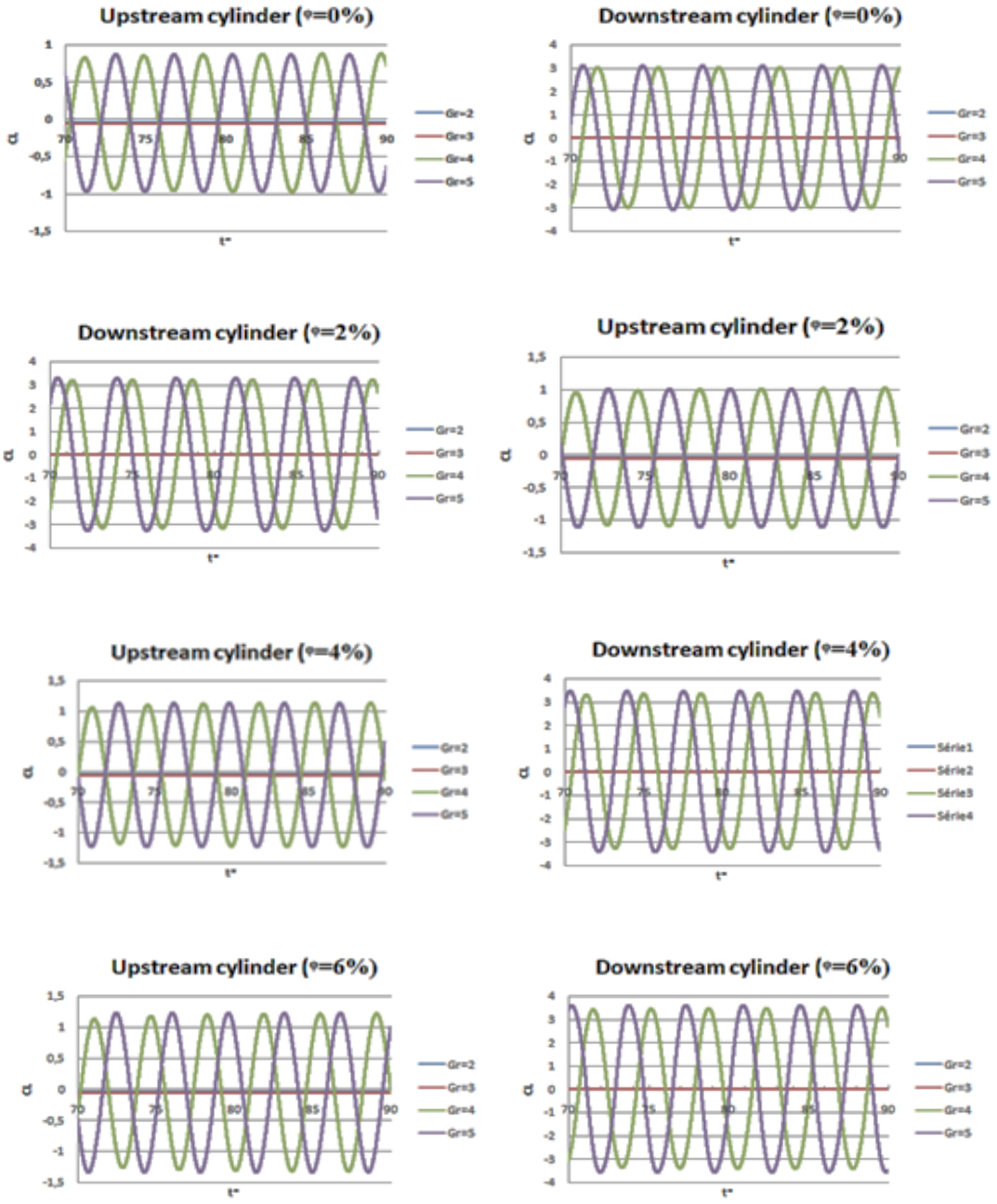

Fig. 7. Lift signals of upstream and downstream cylinders for various gap ratios and volume fractions.

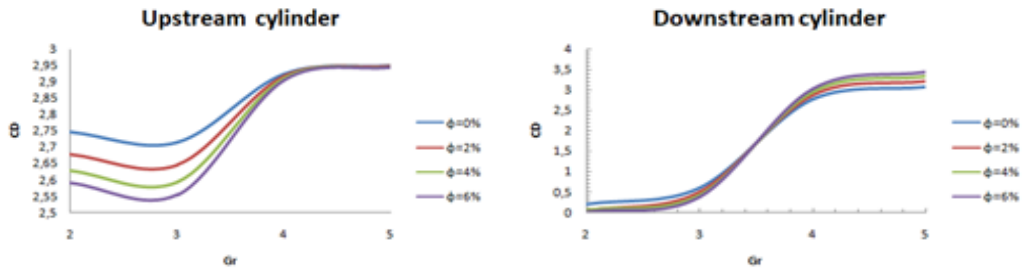

Fig. 8. Drag coefficients of upstream and downstream cylinders for different gap ratios and volume fractions.

5.4 Variation of local nusselt number (nu) with gap ratio and volume fractions

Figure 9 illustrates the variation of the local Nusselt number along the circumferential angle θ for different gap ratios (GR) and nanoparticle volume fractions (ϕ). The local Nusselt number represents the convective heat transfer intensity on the surfaces of both the upstream and downstream cylinders. As depicted in the figure, an increase in the nanoparticle concentration enhances the effective thermal conductivity of the nanofluid, which consequently improves the heat transfer rate. This enhancement arises from the intensified interaction between the suspended nanoparticles and the heated surface, leading to higher local heat transfer coefficients.

Furthermore, the thickness of the thermal boundary layer decreases noticeably as the solid volume fraction increases from ϕ = 0 % to ϕ = 6 %. The results confirm that the inclusion of nanoparticles in the base fluid consistently augments the local Nusselt number. Quantitatively, the convective heat transfer rises by approximately 8 % for the upstream cylinder at GR = 4 and by about 28 % for the downstream cylinder under the same conditions when ϕ = 6 %.

It can also be observed that the maximum local Nusselt number occurs near the forward region of both cylinders. Because heat transfer is closely correlated with the flow dynamics, the minimum local heat transfer values appear at the stagnation points on the front and rear sides of the downstream cylinder, where the flow velocity is relatively low for GR = 2 and 3. The distribution pattern of the local Nusselt number on the downstream cylinder closely resembles that of the upstream one for higher gap ratios (GR = 4 and 5). The upstream cylinder shows peak heat transfer around θ = 45° and θ = 360°, whereas the downstream cylinder displays two pronounced maxima at θ ≈ 115° and θ ≈ 240° for GR = 2 and 3, corresponding to regions where the thermal and hydrodynamic boundary layers are at their thinnest.

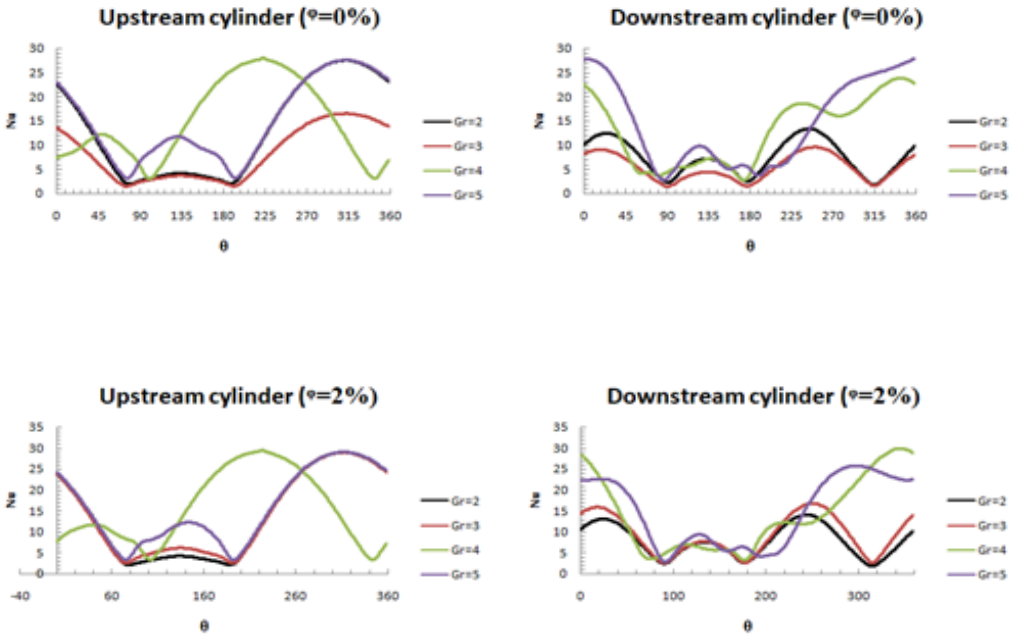

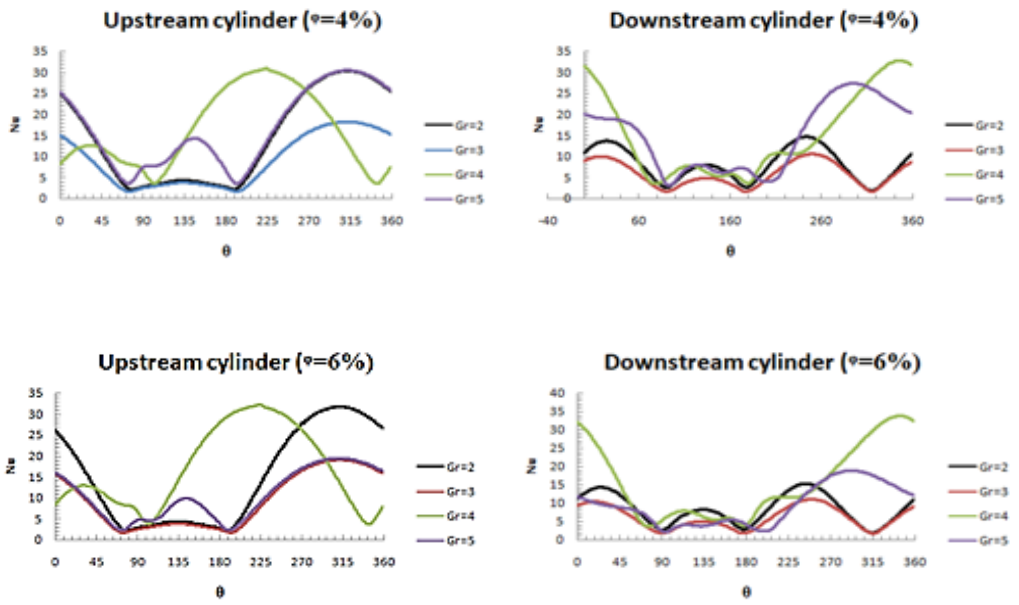

Fig.9. Local Nusselt number of upstream and downstream cylinders for different gap ratios and volume fractions.

5.5 Variation of average nusselt number (nu) with volume fractions and gap ratio

Figure 10 presents the variation of the average Nusselt number for both upstream and downstream cylinders as a function of the gap ratio (GR) and nanoparticle volume fraction (ϕ) at Re = 100. The results indicate that the upstream cylinder consistently exhibits higher average Nusselt numbers compared to the downstream cylinder. For moderate spacing ($2 \leq GR < 4$), the heat transfer from both cylinders increases with the gap ratio, whereas for larger spacings ($GR \geq 4$), the average Nusselt number tends to plateau for the upstream cylinder and slightly decreases for the downstream one.

Additionally, the heat transfer performance improves with increasing nanoparticle concentration, with more pronounced enhancement observed at higher ϕ values. In forced flow conditions and for $GR \leq 4$, the presence of nanoparticles intensifies mixing within the boundary layer, causing the isotherms to flatten near the cylinder surfaces. This effect increases temperature gradients in the bulk fluid, thereby enhancing convective heat transfer from both cylinders at smaller gap ratios. At higher spacings ($GR \geq 4$), nanoparticle agglomeration reduces the effectiveness of convective mixing, resulting in a relatively constant enhancement for the upstream cylinder and a minor decrease for the downstream cylinder.

Overall, the global convective transport is stronger for the upstream cylinder than for the downstream one, with the difference being more significant at smaller gap ratios. As the spacing increases, this disparity diminishes substantially, reflecting the reduced interaction between the cylinder wakes. Although the present geometry and laminar flow conditions are simplified, the results provide fundamental insights into wake-induced heat transfer mechanisms that are relevant to compact heat exchanger elements operating under low-Reynolds-number conditions or during start-up and low-load regimes

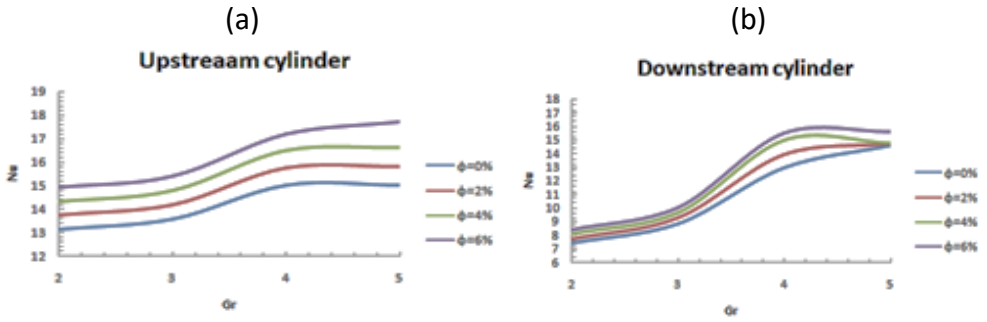

Fig.10. Average Nusselt number of (a) upstream and (b) downstream cylinders for different gap ratios and volume fractions.

The stronger heat transfer enhancement observed for the downstream cylinder is primarily attributed to wake-induced mixing generated by the upstream cylinder. The incoming vortices periodically thin the thermal boundary layer on the downstream cylinder, intensifying convective transport. The presence of nanoparticles further amplifies this effect by enhancing thermal diffusion within the unsteady wake region. As a result, the downstream cylinder experiences a synergistic interaction between vortex shedding and nanofluid thermal properties

The reported percentage enhancements in Nusselt numbers are based on time-averaged quantities obtained after achieving periodic convergence of force and heat transfer signals. Numerical uncertainty is minimized through strict convergence criteria, with residuals reduced below 10^{-6} for momentum and energy equations. Remaining uncertainties may arise from discretization errors, modeling assumptions associated with the single-phase nanofluid approach, and the choice of constant thermophysical properties.

he observed enhancement trends in the present study are consistent with previous numerical investigations of nanofluid flow around isolated cylinders and bluff bodies, which reported improved heat transfer due to increased effective thermal conductivity. However, unlike isolated-cylinder studies, the present results highlight that wake interference plays a dominant role in amplifying heat transfer on the downstream cylinder. Minor discrepancies in enhancement levels compared to earlier studies can be attributed to differences in confinement, cylinder interaction, and flow regime

6. Conclusions

This study presents a numerical investigation of Cu–water nanofluid flow and heat transfer around two tandem cylinders in a semi-confined channel at Re = 100, for gap ratios ranging from GR = 2 to 5 and nanoparticle volume fractions ϕ = 0–6%. The main findings can be summarized as follows:

- Flow regimes: The flow remains steady without vortex shedding for GR < 4. For GR ≥ 4, unsteady vortex shedding occurs, forming well-defined Kármán vortex streets.
- Critical spacing: The transition from steady to unsteady flow is observed at a critical gap ratio of approximately 3.9, which is unaffected by the addition of nanoparticles.
- Hydrodynamic forces: The downstream cylinder experiences stronger unsteady lift and drag forces compared with the upstream cylinder due to wake interactions.
- Heat transfer distribution: The upstream cylinder consistently exhibits higher average Nusselt numbers, while the downstream cylinder reaches approximately 50% of the upstream cylinder's heat transfer.

- Effect of nanoparticles: Incorporating Cu nanoparticles enhances convective heat transfer. At ϕ = 6%, the average Nusselt number increases by around 8% for the upstream cylinder and by 28% for the downstream cylinder relative to pure water.
- Overall enhancement: Across all gap ratios, the presence of nanofluids leads to an overall improvement of up to 15% in the average Nusselt number.

These results demonstrate that nanofluid suspensions can substantially improve convective heat transfer in compact heat exchanger configurations while preserving the critical spacing behavior observed for conventional fluids.

Future studies should extend the present analysis to higher Reynolds numbers and turbulent flow regimes to assess the robustness of the observed enhancement mechanisms under practical operating conditions. Incorporating two-phase nanofluid models that account for particle slip, agglomeration, and temperature-dependent properties would further improve physical realism. In addition, experimental validation and investigations of multi-cylinder arrays representative of compact heat exchanger cores are recommended to directly link the present findings to industrial applications

References

[1] Igarashi, Tamotsu. 1981. "Characteristics of the Flow around Two Circular Cylinders Arranged in Tandem. 1st Report." *Bulletin of the JSME* 24 (188): 323–331. https://doi.org/10.1299/jsme1958.24.323.

[2] Igarashi, Tamotsu. 1984. "Characteristics of the Flow around Two Circular Cylinders Arranged in Tandem: 2nd Report. Unique Phenomenon at Small Spacing." *Bulletin of the JSME* 27 (233): 2380–2387. https://doi.org/10.1299/jsme1958.27.2380.

[3] Zdravkovich, M. M. 1987. "The Effects of Interference between Circular Cylinders in Cross Flow." *Journal of Fluids and Structures* 1 (2): 239–261. https://doi.org/10.1016/S0889-9746(87)90355-0.

[4] Chung, Y. J., and S.-H. Kang. 2000. "Laminar Vortex Shedding from a Trapezoidal Cylinder with Different Height Ratios." *Physics of Fluids* 12 (5): 1251–1254. https://doi.org/10.1063/1.870376.

[5] Rosales, J. L., A. Ortega, and J. A. C. Humphrey. 2001. "A Numerical Simulation of the Convective Heat Transfer in Confined Channel Flow Past Square Cylinders: Comparison of Inline and Offset Tandem Pairs." *International Journal of Heat and Mass Transfer* 44 (3): 587–603. https://doi.org/10.1016/S0017-9310(00)00113-7.

[6] Ding, H., C. Shu, K. S. Yeo, and D. Xu. 2007. "Numerical Simulation of Flows around Two Circular Cylinders by Mesh-Free Least Square-Based Finite Difference Methods." *International Journal for Numerical Methods in Fluids* 53 (2): 305–332. https://doi.org/10.1002/fld.1281.

[7] Mahir, Necati, and Zekeriya Altaç. 2008. "Numerical Investigation of Convective Heat Transfer in Unsteady Flow Past Two Cylinders in Tandem Arrangements." *International Journal of Heat and Fluid Flow* 29: 1309–1318. https://doi.org/10.1016/j.ijheatfluidflow.2008.05.001.

[8] Sohankar, A., and A. Etminan. 2009. "Forced-Convection Heat Transfer from Tandem Square Cylinders in Cross Flow at Low Reynolds Numbers." *International Journal for Numerical Methods in Fluids* 60 (7): 733–751. https://doi.org/10.1002/fld.1909.

[9] Sumner, D. 2010. "Two Circular Cylinders in Cross-Flow: A Review." *Journal of Fluids and Structures* 26 (6): 849–899. https://doi.org/10.1016/j.jfluidstructs.2010.07.001.

[10] Jiang, Ren-Jie, and Jian-Zhong Lin. 2012. "Wall Effects on Flows Past Two Tandem Cylinders of Different Diameters." *Journal of Hydrodynamics* 24 (1): 1–10. https://doi.org/10.1016/S1001-6058(11)60212-6.

[11] Harichandan, A. B., and A. Roy. 2012. "Numerical Investigation of Flow Past a Single and Tandem Cylindrical Bodies in the Vicinity of a Plane Wall." *Journal of Fluids and Structures* 33: 19–43. https://doi.org/10.1016/j.jfluidstructs.2012.04.006.

[12] Dhiman, Amit, and Mudassir Hasan. 2013. "Flow and Heat Transfer over a Trapezoidal Cylinder: Steady and Unsteady Regimes." *Asia-Pacific Journal of Chemical Engineering* 8 (3): 433–446. https://doi.org/10.1002/apj.1678.

[13] Rajpoot, Rajendra S., K. Anirudh, and S. Dhinakaran. 2021. "On the Effects of Orientation on Flow and Heat Transfer from a Semi-Circular Cylinder near a Stationary Wall." *Case Studies in Thermal Engineering* 26: 100967. https://doi.org/10.1016/j.csite.2021.100967.

[14] Gupta, Rakesh Kumar, Avinash Chandra, and Raj Kumar Gupta. 2023. "Mixed Convection from Tandem Semi-Circular Cylinders Arranged in a Vertical Channel." *Iranian Journal of Chemistry and Chemical Engineering* 42 (6). https://doi.org/10.30492/ijcce.2022.560950.5555.

[15] Abdelhamid, Talaat, Ahmed G. Rahma, Md. Mahbub Alam, Rongliang Chen, Md. Islam, Qiang Zhou, and Hongjun Zhu. 2023. "Heat Transfer and Flow around Curved Corner Cylinder: Effect of Attack Angle." *SN Applied Sciences* 5: 163. https://doi.org/10.1007/s42452-023-05377-w.

[16] Mahmoodi, Mostafa. 2011. "Mixed Convection inside Nanofluid-Filled Rectangular Enclosures with Moving Bottom Wall." *Thermal Science* 15 (3): 889–903. https://doi.org/10.2298/TSCI101129030M.

[17] Soltanipour, Hosseinali, Parisa Choupani, and Iraj Mirzaee. 2012. "Numerical Analysis of Heat Transfer Enhancement Using γ-Al_2O_3 Nanofluid and Longitudinal Ribs in a Curved Duct." *Thermal Science* 16 (2): 469–480. https://doi.org/10.2298/TSCI1107190285.

[18] Fallah, Keivan, Atena Ghaderi, Nima Sedaghatizadeh, and Mohammad Hossein Borghei. 2017. "Simulation of Natural Convection Heat Transfer Using Nanofluid in a Concentric Annulus." *Thermal Science* 21 (3): 1275–1286. https://doi.org/10.2298/TSCI150118078F.

[19] Dharmaraj, Arumuga Perumal, Kumar Gundavarapu V. S., and Anoop K. Dass. 2014. "Lattice Boltzmann Simulation of Flow over a Circular Cylinder at Moderate Reynolds Numbers." *Thermal Science* 18 (4): 1235–1246. https://doi.org/10.2298/TSCI110908093A.

[20] Mahfouz, F. M., and H. M. Badr. 2000. "Forced Convection from a Rotationally Oscillating Cylinder Placed in a Uniform Stream." *International Journal of Heat and Mass Transfer* 43: 3093–3104. https://doi.org/10.1016/S0017-9310(99)00326-9.

[21] Etminan-Farooji, Vahid, Ehsan Ebrahimnia-Bajestan, Hamid Niazmand, and Somchai Wongwises. 2012. "Unconfined Laminar Nanofluid Flow and Heat Transfer around a Square Cylinder." *International Journal of Heat and Mass Transfer* 55: 1475–1485. https://doi.org/10.1016/j.ijheatmasstransfer.2011.10.030.

[22] Azad, Ali, Ali Akbar Abbasian Arani, Ali Arefmanesh, and Rahim Shamsoddini. 2025. "Analysis of Nanofluid Flow and Heat Transfer inside a Channel Using Smoothed Particle Hydrodynamics." *International Journal of Thermofluids* 25: 100955. https://doi.org/10.1016/j.ijft.2024.100995.

[23] Sarkar, Sandip, Suvankar Ganguly, and G. Biswas. 2012. "Mixed Convective Heat Transfer of Nanofluids Past a Circular Cylinder in Cross Flow in an Unsteady Regime." *International Journal of Heat and Mass Transfer* 55: 4783–4799. https://doi.org/10.1016/j.ijheatmasstransfer.2012.04.046.

[24] Xuan, Yimin, and Qiang Li. 2003. "Investigation on Convective Heat Transfer and Flow Features of Nanofluids." *Journal of Heat Transfer* 125: 151–155. https://doi.org/10.1115/1.1532008.

[25] Ridha, Mebrouk, Kadja Mahfoud, Lachi Mohamed, and Stéphane Fohanno. 2016. "Numerical Study of Natural Turbulent Convection of Nanofluids in a Tall Cavity Heated from Below." *Thermal Science* 20 (6): 2051–2064. https://doi.org/10.2298/TSCI150225089M.

[26] Darvishyadegari, Mohsen, and Rahim Hassanzadeh. 2012. "Numerical Simulation of Fluid Flow and Forced Convection Heat Transfer from Tandem Circular Cylinders Using the Overset Grid Method." *Journal of Fluids and Structures* 28: 309–327.

[27] Dwivedi, A. R., and A. K. Dhiman. 2019. "Flow and Heat Transfer Analysis around Tandem Cylinders: Critical Gap Ratio and Thermal Cross-Buoyancy." *Journal of the Brazilian Society of Mechanical Sciences and Engineering* 41: 487. https://doi.org/10.1007/s40430-019-1980-8.

[28] Zdravkovich, M. M., and D. L. Pridden. 1977. "Interference between Two Circular Cylinders: Series of Unexpected Discontinuities." *Journal of Wind Engineering and Industrial Aerodynamics* 2 (3): 255–270. https://doi.org/10.1016/0167-6105(77)90026-5.

[29] Brinkman, H. C. 1952. "The Viscosity of Concentrated Suspensions and Solutions." *The Journal of Chemical Physics* 20: 571–581. https://doi.org/10.1063/1.1700493.